Metal Phase, Electron Density, Textural Properties, and Catalytic Activity of CoMo Based Catalyst Applied in Hydrodeoxygenation of Oleic Acid

Khoirina Dwi Nugrahaningtyas
Dept. of Chemistry, Faculty of Mathematics and Natural Sciences, Sebelas Maret University

Rujito S.R. Suharbiansah
Institute of Chemical Technology, Faculty of Chemistry and Mineralogy, Leipzig University

Witri Wahyu Lestari
Dept. of Chemistry, Faculty of Mathematics and Natural Sciences, Sebelas Maret University

Rahmawati, Fitria
Dept. of Chemistry, Faculty of Mathematics and Natural Sciences, Sebelas Maret University

Metal Phase, Electron Density, Textural Properties, and Catalytic Activity of CoMo Based Catalyst Applied in Hydrodeoxygenation of Oleic Acid

Khoirina Dwi Nugrahaningtyas[1,*], Rujito S.R. Suharbiansah[2], Witri Wahyu Lestari[1], Fitria Rahmawati[1]

[1]Dept. of Chemistry, Faculty of Mathematics and Natural Sciences, Sebelas Maret University, Jl. Ir Sutami No 36A, Surakarta, Indonesia

[2]Institute of Chemical Technology, Faculty of Chemistry and Mineralogy, Leipzig University, Linnéstraße 3, 04103, Leipzig, Germany

*Author to whom correspondence should be addressed:
E-mail: khoirinadwi@staff.uns.ac.id

Abstract: Vegetable oil is a promising alternative fuel source, but the high content of oxygenate compounds reduces its performance. Therefore, in this study, a Co- and Mo-based catalyst was synthesized with Ultra Stable Y-zeolite (USY), Mordenite (MOR), or activated Indonesian natural zeolite (ANZ) as supports, to reduce the oxygen content of the vegetable oil model compounds. The type of metal phase is similar in each support, except for the MoO_3 phase, which is disappeared in AZN. The addition of metal causes a change in electron density and reduces the specific surface area. Meanwhile, CoMo/USY showed the best performance with a gasoline fraction selectivity of 85.7%.

1. Introduction

The petroleum component consists of hydrocarbon compounds and non-hydrocarbon compounds with 83-87% carbon content, 10-14% hydrogen, 0.05-6% sulfur, 0.05-1.5% oxygen, and 0.1-2% nitrogen. Based on the constituent components of petroleum, impurities will interfere with the quality of the fuel. Meanwhile, the reaction of vegetable oil/animal fat conversion through transesterification can produce fuel[1]. However, the fuel still contains many impurities in the form of oxygenated compounds, so the quality of the fuel produced is still low[2]. Therefore, the fuel quality from vegetable oils/animal fats must be improved. One way is through the process of hydrodeoxygenation (HDO)[3]. The HDO reaction reduces the oxygen content that binds to hydrocarbon compounds. HDO can be done in two ways, namely thermal HDO and catalysis. HDO with catalysis will give good results at lower temperatures and pressures[4]. These properties are fulfilled by metal-supported catalysts of metals carried on solid carriers such as silica-alumina, alumina, and zeolite.

Murata and colleagues have studied the effect of carrier variations, namely gamma-alumina and several types of zeolites such as USY, MOR, and ZSM-5 on the transformation of ethanol into olefin[5]. It is known that the highest ethanol conversion is produced from catalysts with USY supporting material, which is 72.1%. The supporting material used by Murata is synthetic materials. Meanwhile, natural zeolite is an excellent material for supporting metals in preparing of catalysts. Natural zeolites are easy to find in the United States, Japan, Cuba, the Soviet Union, Italy, Czechoslovakia, Hungary, Bulgaria, South Africa, Yugoslavia, Mexico, Korea, and Indonesia[6]. In Indonesia, natural zeolite reserves are more than 205.82 million tonnes. The most abundant zeolite deposits in Java are Central Java (Wonosari, Klaten), West Java (Bogor, Tasikmalaya, Sukabumi), and East Java (Bayah)[7].

The metals commonly used in the petroleum industry are Co, Mo, Pt, and Pd [8]. Mo metal has an active function for deoxygenation [9]. Such as, in the hydrogenolysis reaction, Mo metal will react with the phenol hydroxyl molecule by releasing H_2O and forming benzene products [10]. While metals Co, Pt, and Pd play a role in the hydrogenation reaction [11,12]. Shim and colleagues investigated the decarboxylation of oleic acid using an unsupported CoMo catalyst. The catalyst with the highest $CoMoO_4$ content produced the optimum yield of oleic acid decarboxylation, which was 88%. Because CoMoO4 is easier to remove oxygenate compounds than MoO_3 or Co_3O_4 [6]. Our previous study showed that the Co/Mo ratio variation causes the

difference in composition of the metal phases Co, Mo, CoMo, MoO_3, Co_3O_4, and $CoMoO_4$[13].

The choice of catalyst synthesis method needs to be considered to get a good catalyst character. According to Soltanali and coworkers, the preparation of Cu/HZSM-5 using the impregnation method produced a catalyst with a longer lifetime than the ion exchange method[14]. So in this study, the CoMo/USY, CoMo/MOR, and CoMo/ANZ catalysts were prepared using the impregnation method. The catalysts obtained were tested in the HDO reaction of oleic acid for the performance of CoMo/USY, CoMo/MOR, and CoMo/ANZ catalysts. Oleic acid was chosen as a decoy compound because of its molecular structure representing compounds of vegetable oil components and animal fats. In our present paper, we studied the effects of three types of supports, namely USY, MOR, and Indonesian natural zeolite, on catalytic properties, including Metal Phase, Electron Density, textural Properties, and Catalytic Activity of CoMo Based Catalyst for HDO oleic acid.

2. Materials and Methods

2.1 Materials

The first supporting material used in this research is H-USY obtained from the calcination of HSZ-341 (Tosoh Corporation, Japan) at 500ºC under N2 flow for 1 hour. Without further treatment, the second type of support is MOR HS-690 (Wako Pure Chemical, China). Meanwhile, the third support is the natural zeolite from Wonosari Yogyakarta, Indonesia. Other chemicals used are Ammonium heptamolybdate tetrahydrate, Cobalt (II) nitrate hexahydrate, and oleic acid (pro analysis level) purchased from Merck (Germany).

2.2 Procedure

2.2.1 Preparation of Activated Natural Zeolite (ANZ)

Natural zeolite is immersed in deionized water while stirred with a magnetic stirrer for 24 hours at room temperature, followed by filtration, and dried at a temperature of 100ºC for 24 hours. Amount of 5 g natural zeolites was immersed in 125 mL of 6 N HCl solution for 30 minutes at a temperature of 50 ºC while stirred, followed by filtered and washed until free of Cl ions. Then, the obtained sample was dried at a temperature of 130 ºC for 3 hours, followed by soaked in NH_4Cl 1N solution at a temperature of 90 ºC for one week, then washed until free of Cl ions. The next step is filtered, followed by calcined at a temperature of 550 ºC for 3 hours under N_2 gas at a flow rate of 10 mL/min. The obtained sample was named natural active zeolite (ANZ), and the next step was used as a supported catalyst.

2.2.2 Preparation of CoMo/USY, CoMo/MOR, CoMo/ANZ

The CoMo/USY catalyst was prepared by the co-impregnation method, in which some H-USY was added with ammonia solution, then 10 g of H-USY was immersed in a solution of ammonium heptamolybdate tetrahydrate (8% w/w) and Cobalt (II) nitrate hexahydrate (2% w/w). The solution refluxed at a temperature of 60 °C for 2 hours, followed by filtering. Furthermore, the obtained residue was dried with a rotary evaporator at 200 mbar pressure on the temperature of 48 °C up to form a powder.

The sample powder was activated by calcination and reduction processes. The calcination process is carried out by heating the sample at 550 °C for 3 hours under N gas, followed by the reduction process at 400 °C for 2 hours under H_2 gas. The same steps are repeated to obtain CoMo/MOR and CoMo/ANZ catalysts.

2.2.3 Catalytic test on HDO reaction of oleic acid

Oleic acid is put into the batch reactor together with the catalyst. Then the reactor is connected to hydrogen gas. The furnace is heated to 364 °C with a constant hydrogen gas pressure at 1 or 18 Bar for 1 hour. The obtained product is stored in a container and analyzed using GC-MS. The same steps are repeated for the Thermal, USY, CoMo/USY, MOR, CoMo/MOR, ANZ, CoMo/ANZ reactions.

Based on the number of peaks in the GC chromatogram, the number of compounds contained in the sample can be analyzed. While the names of each compound are interpreted based on fragmentation using the GC-MS database library approach. The conversion, yield of product and catalyst selectivity are calculated based on equations 1, 2, and 3.

$$Conversion(\%) = \frac{Volume\ of\ feed - Remaining\ Volume}{Volume\ of\ Feed} \quad eq.1$$

$$Yield\ of\ Product(\%) = Area\ Product(\%) \times \frac{Volume\ of\ Product}{Volume\ of\ Feed} \quad eq.\ 2$$

$$Selectivity\ of\ k(\%) = \frac{Yield\ of\ k(\%)}{Yield\ of\ Product(\%)} \quad eq.3$$

k is gasoline (C5 – C8) or kerosene (C9 – C16).

2.2.4 Characterization methods

Structural characterization to determine the crystalline phase was carried out by using X-ray Powder Diffraction Philips type X'Pert, using monochromatic Cu Kα radiation. Measurement conditions are in the range of 2θ range = 2 – 45°, 2θ step = 0.021º, acquisition time = 2.5 s per step. The crystal structure is analyzed by the Rietveld method, which is widely applied to extract detailed crystal structure information from X-ray diffraction data. Improvements were made using the Le Bail calculation method to measure the phases of the sample composition by comparing experimental XRD data complete with standard diffraction patterns. Experimental parameters were refined the instrument zero, scale factor, the lattice parameters, and the peak shape parameters u, v, w, y0, and y1, respectively. Each refinement was conducted at 30 cycles.

Analysis of specific surface area, pore-volume, and average pore radius performed using Surface Area Analyzer (SAA) NOVA 1200e. Data on pressure changes

(P/P_0) and N_2 gas volume at the adsorption and desorption isotherms are used to calculate specific surface area, total pore volume, and average pore radius using the BET method.

The amount of oleic acid conversion to HDO products, namely HDO activity, is calculated based on GC-MS data. While, the number of peaks on the gas chromatogram indicated the number of compounds. Furthermore, the name of the compound is interpreted based on fragmentation using the MS database libraries approach. Then, the selectivity of HDO products is calculated based on the number of shorter hydrocarbon chain products and is divided into two types of selectivity, namely gasoline and kerosene selectivity. HDO selectivity is classified based on differences in the number of hydrocarbon chains, namely the gasoline (C5 - C8) and paraffin (C9 - C16) fraction.

3. Results and Discussion

3.1 XRD Analysis and Le Bail refinement

Based on the suitability of the diffraction pattern between the catalyst and the support (Figure 1), it is known that the metal impregnation process does not change the diffraction pattern of each support, either USY, MOR, or ANZ. However, quantitative analysis needs to be carried out to determine changes in cell parameters and sample crystallinity. One of the quantitative analyses that can be done is refinement with Rietica software and using the Le Bail method[13,15,16].
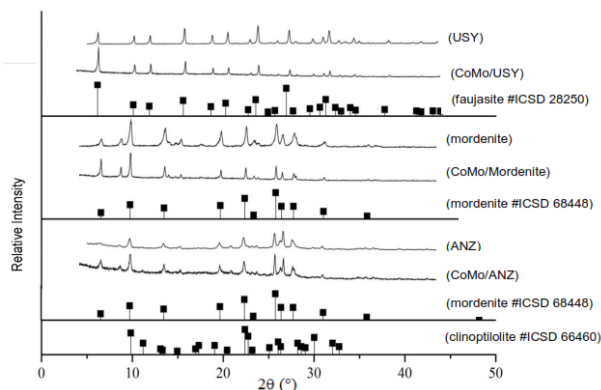

Fig. 1: Diffractogram pattern of USY, CoMo/USY, MOR, CoMo/Mordenit, ANZ, and CoMo/ANZ with simulated pattern faujasite #ICSD 28250, clinoptilolite #ICSD 66460, mordenite #ICSD 68448.

The intensity decrease of the characteristic peak indicate that metal loading caused a crystallinity decrease of all catalysts (Fig. 1). At the same time, the decrease in the value of the residual factor indicates an acceptable standard. So based on further analysis with Rietica software, it was found that theCoMo/USY sample has a cubic lattice structure with space group F d-3 m z, and the characteristic lengths of each crystal axis x, y, and z are always the same (x = y = z). It was found that CoMo/USY contains phases namely Zeolite Y (ICSD #31542), CoO (ICSD #9865), MoO_3 (ICSD #36167), CoMoO4 (ICSD #281235), Co

(ICSD #41507), Mo (ICSD #173127), and CoMo (ICSD #624215) (Table 1). Meanwhile, as stated in our previous paper, CoMo/MOR has a phase similar to CoMo/USY except for the supporting phase, namely CoMo/MOR catalyst has a MOR support phase (ICSD #68448). While, the CoMo/MOR sample has an orthorhombic lattice structure with a C M C M space group, having an axis length x = y ≠ z [13].

The analysis results of the CoMo/ANZ catalyst obtained that the catalyst contains a support phase of MOR (ICSD #68448), MOR (ICSD #68447), and clinoptilolite (ICSD #66460). The lattice structure is orthorhombic with the space group C M C M and the axis length of x = y ≠ z. In addition, the CoMo/ANZ catalysts contain phases of CoO (ICSD #9865), $CoMoO_4$ (ICSD #281235), Co (ICSD #41507), Mo (ICSD #173127), and CoMo (ICSD #624215).

Table 1. The cell parameters of CoMo/USY, CoMo/MOR, CoMo/ANZ catalysts.

Standards	Weight percentage of		
	CoMo/ USY	CoMo/ MOR	CoMo/ ANZ
Faujasite ICSD #31542	11.24	-	-
Y Zeolite ICSD #28250	88.15	-	-
MOR ICSD #68448	-	87.07	67.81
Clinoptilolite ICSD #66460	-	-	24.21
CoO ICSD #9865	0.12	1.31	1.68
MoO_3 ICSD #36167	0.30	6.23	-
$CoMoO_4$ ICSD #281235	0.10	3.62	3.09
Co ICSD #41507	0.02	0.23	1.90
Mo ICSD #173127	0.06	0.87	0.74
CoMo ICSD #624215	0,02	0.67	0.57
Cell Volume ($Å^3$)	147.60	2742.81	2742.82
Rp	5.66	5.99	6.80
Rwp	6.92	6.20	7.41

Fourier density mapping can describe a material's structure and electron density in detail[17,18]. All of the Fourier mappings showed that the electron density (anion area) increases after metal impregnation (Fig 2). In USY, the highest electron density (yellowish-green circle) is ascribed to the main constituents of USY, namely Si and Al metals. After metal loading, there was a significant change in electron density, so it was assumed that it came from metals in the MoO_3, CoO, $CoMoO_4$, Co, and Mo phases and were dispersed on the surface of the catalyst. In MOR, the region of the highest electron density is assumed to come from the main constituents of MOR, namely Si and Al metals. After the metal impregnation process, the increase

in density is thought to also come from the content of metal phases such as CoO, MoO_3, $CoMoO_4$, Co, and Mo. Then the ANZ consist of two types of Si/Al content, namely clinoptilolite and MOR carrier, so that the electron density area is relatively low. However, the attachment of metal to ANZ also causes a change in its electron density.

The Fourier mappings showed that the electron density (anion area) increases after metal impregnation. Based on this Fourier plot, we also know changes in the location or anion point before and after impregnation. It is becoming a clue to the location of metal after the impregnation process.

This Fourier plot density analysis needs to be supported by three-dimensional mapping analysis because the three-dimensional analysis can determine changes in electron density in more detail. Three-dimensional Fourier plot mapping is presented in Figure 3. These results also indicated that metal particles such as Co, Mo, $CoMoO_4$, CoO, and MoO_3 successfully enter the crystal lattice of the support.
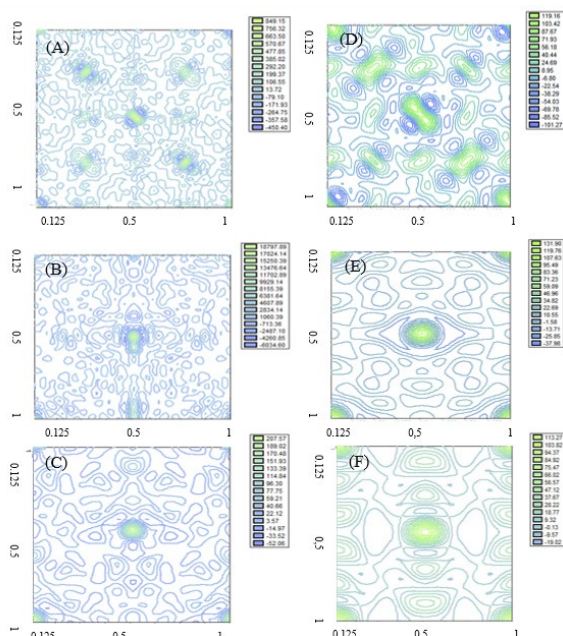

Fig 2: The 2D Fourier Plot Mapping of USY (A), CoMo/USY (B), MOR (C), CoMo/MOR (D), ANZ (E), and CoMo/ANZ (F).

A metal phase in each catalyst can significantly change the Fourier mapping pattern. According to the emergence of new density areas (reddish yellow) in CoMo/USY and CoMo/MOR. The new density region is assumed to originate from the metal embedded in the sample (Figure 3). This prediction is in good agreement with the results of quantitative analysis based on Rietveld's molar calculations (Table 1). The presence of a high or low Fourier frequency relationship can predict the density distribution pattern from various x, y, and z axes. The phase content of metal inside the catalyst will produce a more dense and dynamic electron illustration than the oxygen atom surrounding the equatorial line on the x, y, and z axes[18]. However, it needs to be proven by further analysis of the crystallinity profile (Table 2).
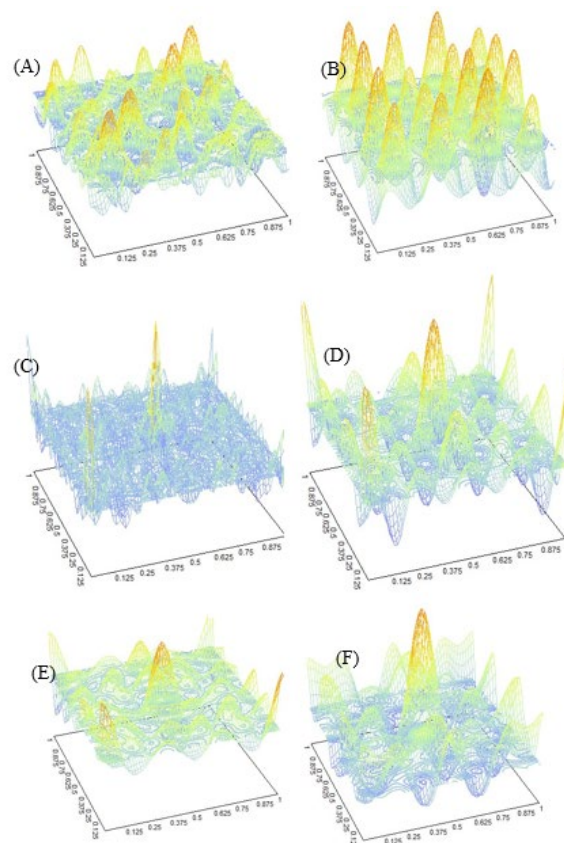

Fig 3: Three dimensional Fourier plot mapping of USY (A), CoMo/USY (B), MOR (C), CoMo/MOR (D), ANZ (E), and CoMo/ANZ (F).

Analysis of the Full width at Half Maximum (FWHM) value can use to find out principal information related to the surface state of the material, such as crystallinity, crystal size, dislocation density, and residual stress[19,20]. Table 2 showed that the FWHM decreased after the metal impregnation processes. It indicated the improvement in the crystallinity[23], crystallite size[25], structural disorder, and relaxation of tensile stress[27] after metal loading.

Table 2. Crystallinity profile of USY, MOR, and ANZ.

Sample	2θ (º)	Intensity	FWHM
USY	15.80; 23.87; 27.30	844.46; 1000; 750.77	0.16; 0.2; 0.2
CoMo/USY	15.83; 23.90; 27.34	537.72; 422.42; 253.43	0.15; 0.12; 0.15
MOR	9.82; 22.54; 25.87	1000; 774.82; 900.60	0.2; 0.24; 0.24
CoMo/MOR	9.82; 22.50; 25.84	1000; 452.65; 512.04	0.15; 0.15; 0.12
ANZ	9.72; 25.67; 26.61	530.37; 858.95; 1000	0.24; 0.18; 0.12
CoMo/ANZ	9.65; 25.58; 26.52	502.74; 857.96; 1000	0.26; 0.2; 0.2

Meanwhile, the CoMo/ANZ diffractogram shows that the crystal size increase after the impregnation process, linear with the increase in the FWHM value. While, an increase in the FWHM value also indicated a reduction of

hardness, crystallinity, and point defects but increased the mobility of the sample grain boundaries and the presence of tensile stress [20,21].

3.2 Textural Properties

Further analysis was performed with Surface Area Analyzer. Surface area analysis was determined to investigate the effect of Co and Mo impregnation on the textural properties of catalysts, such as the specific surface area, pore shape, pore size, and pore distribution. The CoMo/USY, CoMo/MOR, CoMo/ANZ adsorption-desorption curves are shown in Figure 4, and the catalyst-texture data are presented in Table 3.

Figure 4 shows the isotherm curve of the physisorption and the Hysteresis Loop phenomenon. According to IUPAC, the hysteresis loop phenomenon occurs due to multilayer/capillary condensation caused by increased pore size to more than several times the molecular diameter. On the other hand, the average pore size of the supporting material has an essential role in the catalysis process. This study measured the average pore radius using the BJH (Barrett-Joyner-Halenda) method. Based on the IUPAC classification, it was found that CoMo/USY, CoMo/MOR, and CoMo/ANZ have mesoporous structures, type IV adsorption isotherms, and type H1 hysteresis loops. The type H1 hysteresis loop indicates a complex material containing a mixture of nano, micro, and mesopores. Meanwhile, the stepdown characteristic of the desorption branch indicates micropore filling followed by multilayer physisorption and capillary condensation[22]. The adsorption isotherm profile analysis showed that the three supports had the same properties. Namely, the metal-support synergism had no impact on the pore structure of the support.
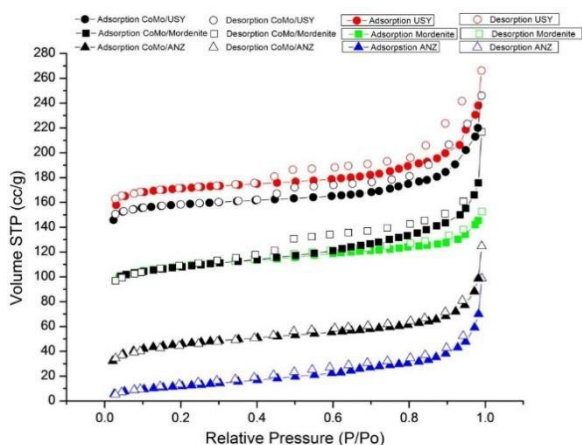

Fig 4: The desorption adsorption curve of USY, MOR, ANZ, CoMo/USY, CoMo/MOR, and CoMo/ANZ

The hysteresis loop of the CoMo/ANZ adsorption isotherm curve follows type D, which is a loop with a flat adsorption isotherm curve, and the desorption isotherm curve tends to follow the adsorption curve. This loop shows that the active natural zeolite pore shape is pointed according to the micropore size type.

The addition of Co and Mo metals into the support results in smaller pore radii due to uneven metal dispersion, metal aggregates that cover the surface pores, or cavities in the catalyst, which causes the measured surface area to be not optimal. At the same time, the reduction of the pore size of the support is due to the overlap of the amount of metal in the support. According to Table 3, it is known that only the specific surface area of CoMo/ANZ was increased, whereas in CoMo/USY and CoMo/MOR were decreased. The phenomenon is due to ANZ having a larger average pore size, so the metal can insert into the pore to form a new pore with a small surface area and average pore size. The shrinking of the average pore radius evidenced this phenomenon, and the rise of total pore volume on CoMo/ANZ indicated the metal was on the supporting material surface to form a new pore.

Table 3. The specific surface area, average pore size, and total pore volume of the catalyst.

Catalyst	Specific surface area (m²/g)	Average pore size (Å)	Total pore volume (cc/g)
USY	506.53	14.05	0.33
MOR	350.48	13.92	0.23
ANZ	47.54	66.83	0.15
CoMo/USY	497.00	16.22	0.38
CoMo/MOR	346.16	19.89	0.33
CoMo/ANZ	153.75	25.60	0.19

Meanwhile, the analysis results on CoMo/USY and CoMo/MOR catalysts showed that the addition of metal caused the specific surface area of the catalyst to decrease, but the average pore size and total pore volume increased. The decrease in surface area is possible due to the large number of metal aggregates covering the mouth of the pores or cavities. Dispersion of metal into the supporting pores can also cause the destruction of the old pore structure and the formation of new pores. However, the surface area of the catalyst in this study was much higher than the dolomite transition metal catalyst synthesized by Azri et al.[23].

All catalysts showed distributed pore sizes in 15-30 A diameter, indicating that each sample had a macropore type (Fig. 5). The pore size distribution will affect the selectivity of the catalyst. The dominance of large pores indicates that the catalyst is less selective for small reactants/products. Conversely, if tiny diameter pores dominate the pores, the catalyst is selective for small reactants/products. Only CoMo/USY has dominated by tiny diameter pores, which is around 15-20 Å, so it can be estimated that the catalyst will be selective towards small reactants or products.
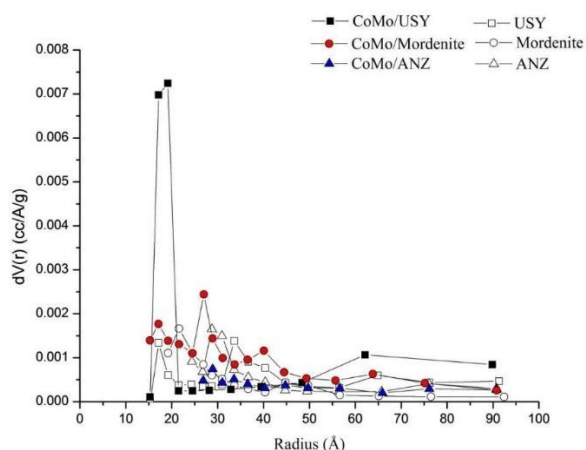
Figure 5. The pore distribution of USY, MOR, ANZ CoMo/USY, CoMo/MOR, and CoMo/ANZ.

3.3 HDO of oleic acid

The amount of oleic acid conversion to HDO products is calculated based on GC-MS data, referred to as HDO activity. At constant of volume and temperature, the increase in hydrogen gas pressure is proportional to hydrogen gas concentration. In the HDO reaction, hydrogen gas is also a reactant, so the higher the concentration of hydrogen gas, it will provide abundant reactants and encourage the formation of products. This theory is proven by the results of the catalytic activity test, which showed a significant increase when the pressure was changed from 1 bar to 18 bar (Fig 6).
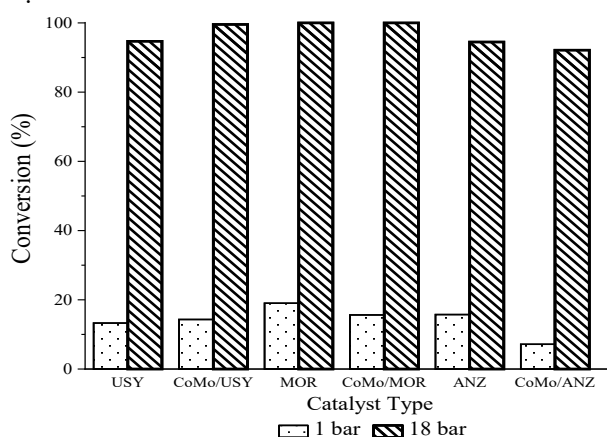

Figure 6. The conversion value of oleic acid with various catalyst types at 364 °C.

The highest conversion in this study reached 100%, namely in the HDO reaction of oleic acid using CoMo/USY, MOR, and CoMo/MOR catalysts and a pressure of 18 bar (Fig 6). The conversion value is greater than the research results by Ayodele and coworkers who carried out the HDO reaction of oleic acid at a pressure of 18 bar with FPtOx/zeolite as a catalyst[24]. The conversion value in this study is also more prominent than the results of Ayanandiran et al.[25] and Lee et al.[26] Ayanandiran and colleagues carried out the HDO reaction of oleic acid at a

pressure of 20.7 bar with a Fe(3)-Cu(13)/SiO$_2$-Al$_2$O$_3$ catalyst, while Lee and friends did the HDO reaction of palmitic acid at a pressure of 35 bar with a NiMo/HZSM-5 catalyst[26]. These results indicate that the CoMo based catalyst is quite effective in dissociating hydrogen molecules and supplying hydrogen atoms to oleic acid so that the reaction pressure of 18 bar is sufficient for hydrogen gas availability.

Table 4. HDO product distribution.

	USY	CoMo/ USY	MOR	CoMo/ MOR	ANZ	CoMo/ ANZ
Alkane						
C$_5$H$_{12}$ isopentane		□	-	-	-	-
C$_5$H$_{10}$O	□	□	-	-	-	□
C$_5$H$_8$	-	□	-	□	-	□
C$_6$H$_{10}$	□	□	-	□	-	□
C$_6$H$_{12}$	□	□	-	□	-	□
C$_6$H$_{14}$	□	□	□	□	□	□
C$_6$H$_{14}$O	-	-	□	□	-	-
C$_7$H$_8$	□	□	□	□	-	□
C$_7$H$_{14}$	□	□	□	□	□	□
C$_7$H$_{16}$	□	□	□	□	□	□
C$_8$H$_{10}$	□	□	□	□	□	□
C$_8$H$_{16}$	□	□	□	□	□	□
C$_8$H$_{18}$	□	□	□	□	□	□
C$_9$H$_{18}$	□	□	□	□	□	□
C$_9$H$_{20}$	□	□	□	□	□	□
C$_{10}$H$_{20}$	□	□	□	□	□	□
C$_{10}$H$_{22}$	□	□	□	□	□	□
C$_{10}$H$_{22}$O	-	-	□	□	-	-
C$_{11}$H$_{24}$	□	□	□	□	□	□
C$_{12}$H$_{24}$	□	-	□	□	□	□
C$_{12}$H$_{26}$	□	□	□	□	□	□
C$_{13}$H$_{28}$	□	-	□	□	□	□
C$_{15}$H$_{32}$O	-	-	-	-	□	□
C$_{14}$H$_{28}$	□	-	□	-	□	□
C$_{15}$H$_{30}$	□	-	□	-	□	□
C$_{16}$H$_{32}$	□	-	□	-	□	□
C$_{16}$H$_{34}$	□	-	□	-	-	-
C$_{17}$H$_{34}$	-	-	-	-	□	-

Noted: □ detected

Synergism between high Fourier density and specific surface area is expected to increase catalytic activity. Unfortunately, this study found no indication of the effect of Fourier density and specific surface area on the catalytic activity. On the other hand, CoMo/ANZ with 25-30 Å pore size is relatively larger than CoMo/USY and CoMo/MOR, that caused the conversion into gasoline, only 28.36%. The compound with carbon chain C9-C16 can be to pass through the cavity surface cavity with a larger pore size so

that caused the selectivity of gasoline compounds will be less optimal. Besides, Fourier density catalysts with a high surface area can generate higher synergies between active sites and feed compounds, resulting in more HDO products being formed. The HDO product distribution are presented in Table 4. It is known that the products with C5-C8 carbon chains increased after the addition of metal.

The selectivity of HDO products is the amount of conversion of oleic acid into shorter hydrocarbon chain products over oleic acid (Fig. 7). CoMo/USY and CoMo/MOR catalysts converted oleic acid into shorter carbon chain compounds than C_5H_{12} and C_5H_8. Then on CoMo/ANZ, there was a significant product selectivity for gasoline (C5-C8 carbon chain). This phenomenon indicates that the addition of metal can increase the presence of active sites on the catalyst.
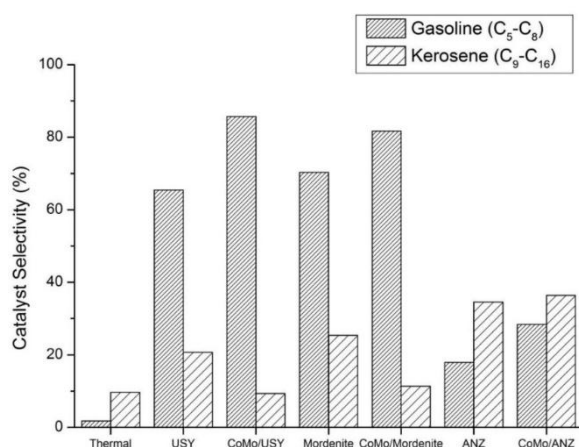

Fig 7. Catalysts Selectivity of Gasoline and Kerosene products.

Each type of catalyst will produce a different percentage of selectivity (Fig. 7). The catalyst character, including pore size, surface area, and metal content, can predict the catalyst selectivity. The CoMo/USY and CoMo/MOR catalysts with a pore size of 15-20 are the most suitable sizes to convert oleic acid into gasoline (carbon chain C5-C8). The prediction is suitable with the research result that showed the conversion of oleic acid to gasoline has increased up to 85.7% in CoMo/USY compared to using without a catalyst (thermal reaction).

The addition of metal could increase the presence of active sites on the catalyst. The proposed mechanisms of the HDO of oleic acid are presented in Figure 8.

The CoMo metal specimens could increase the removal of oxygen groups due to the increase of acid sites on the catalyst's surface. Also, the research results proposed the "promote effect" since the Co metal was added to the Mo metal[27]. So combining bimetallic metal could increase the reaction selectively into several hydrocarbon compounds and components of monoaromatic compounds. Unfortunately, XRD data found the presence of oxide species from metals Co, Mo, and metal alloys. So it is estimated that the presence of these metal oxides causes the catalyst performance to be low, which is indicated by the

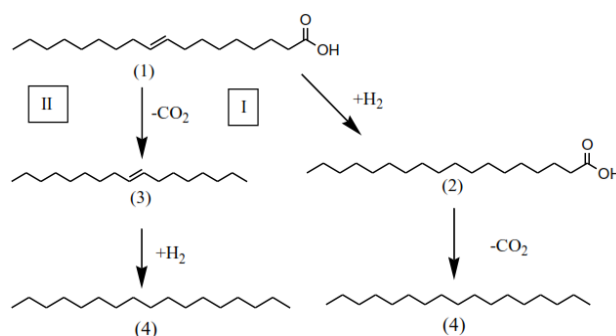catalytic activity value of less than 100%.

Fig 8. The propose of the reaction mechanism of HDO oleic acid. Pathway I adopted from Shim et al.[6] and Pathway II adopted from Ayodele et al.[8].

The reaction mechanism begins with oleic acid $(C_{18}H_{34}O_2)$ (1) undergoing two pathways. Pathway [I] is the decarboxylation of oleic acid to give n-8-heptadecane $(C_{17}H_{34})$ (3) and its isomer. Pathway [II] is the hydrogenation of oleic acid to form an intermediate product, namely stearic acid $(C_{18}H_{36}O_2)$ (2) and its isomer. Furthermore, the intermediate product, namely n-8-heptadecane, is dehydrogenated, or the intermediate product in the form of stearic acid is decarboxylated to give heptadecane (4) and its isomer.

4. Conclusions

Specific surface area results showed the optimum catalyst surface area of CoMo /USY 497 m²/g, the average pore radius of 16.22 Å, and the total pore volume of 0.38 cc/g. Based on Fourier mapping, CoMo/USY was formed a more significant electron density than CoMo/MOR and CoMo/ANZ. The CoMo/USY catalyst was the best in the oleic acid HDO reaction based on the resulting products' activity capability and selectivity.

Nomenclature

HDO	Hydrodeoxygenation
ANZ	Activated Indonesian Natural Zeolite
MOR	Mordenite

References

1) A. Rahman, Nining Betawati Prihantini, and Nasruddin, "Biomass production and synthesis of biodiesel from microalgae synechococcus HS-9 (cyanobacteria) cultivated using bubble column photobioreactors," *Evergreen*, **7** (*4*) 564–570 (2020). doi:10.5109/4150507.

2) J.A. Hidayat, and B. Sugiarto, "Characteristic, structure, and morphology of carbon deposit from

biodiesel blend," *Evergreen*, **7** (*4*) 609–614 (2020). doi:10.5109/4150514.

3) A.E. Coumans, and E.J.M. Hensen, "A model compound (methyl oleate, oleic acid, triolein) study of triglycerides hydrodeoxygenation over alumina-supported NiMo sulfide," *Appl. Catal. B Environ.*, **201** 290–301 (2017). doi:10.1016/j.apcatb.2016.08.036.

4) G. Gottardi, and E. Galli, "Natural zeolites," in: P.l.Wyllie, A.E. Goresy, W von Engelhardt (Eds.), Mineral. Rocks, Springer Berlin Heidelberg, Berlin, Heidelberg, 2019: pp. 1–18. doi:10.1007/ 978-3-642-46518-5.

5) K. Murata, M. Inaba, and I. Takahara, "Effects of surface modification of H-ZSM-5 catalysts on direct transformation of ethanol into lower olefins," *J. Japan Pet. Inst.*, **51** (*4*) 234–239 (2008). https://www.jstage.jst.go.jp/article/jpi/51/4/51_4_234/_pdf (accessed January 31, 2018).

6) J.O. Shim, D.W. Jeong, W.J. Jang, K.W. Jeon, S.H. Kim, B.H. Jeon, H.S. Roh, J.G. Na, Y.K. Oh, S.S. Han, and C.H. Ko, "Optimization of unsupported como catalysts for decarboxylation of oleic acid," *Catal. Commun.*, **67** (*January*) 16–20 (2015). doi:10.1016/j.catcom.2015.03.034.

7) G.M.H.A. Ichsan, K.D. Nugrahaningtyas, D.M. Widjonarko, and F. Rahmawati, "Structure and morphology of the (Ni, Co) Mo/indonesian natural zeolite," *IOP Conf. Ser. Mater. Sci. Eng.*, **578** (*1*) (2019). doi:10.1088/1757-899X/578/1/012009.

8) O.B. Ayodele, O.S. Togunwa, H.F. Abbas, and W.M.A.W. Daud, "Preparation and characterization of alumina supported nickel-oxalate catalyst for the hydrodeoxygenation of oleic acid into normal and iso-octadecane biofuel," *Energy Convers. Manag.*, **88** (2014). doi:10.1016/j.enconman.2014.05.099.

9) J. Horáček, and D. Kubička, "Bio-oil hydrotreating over conventional como & nimo catalysts: the role of reaction conditions and additives," *Fuel*, **198** 49–57 (2017). doi:10.1016/j.fuel.2016.10.003.

10) Y. Romero, F. Richard, and S. Brunet, "Hydrodeoxygenation of 2-ethylphenol as a model compound of bio-crude over sulfided Mo-based catalysts: promoting effect and reaction mechanism," *Appl. Catal. B Environ.*, **98** (*3–4*) 213–223 (2010). doi:10.1016/j.apcatb.2010.05.031.

11) H. Zhang, H. Lin, and Y. Zheng, "The role of cobalt and nickel in deoxygenation of vegetable oils," *Appl. Catal. B Environ.*, **160**–**161** (*1*) 415–422 (2014). doi:10.1016/j.apcatb.2014.05.043.

12) F. Mauriello, H. Ariga-Miwa, E. Paone, R. Pietropaolo, S. Takakusagi, and K. Asakura, "Transfer hydrogenolysis of aromatic ethers promoted by the bimetallic Pd/Co catalyst," *Catal. Today*, **357** 511–517 (2020). doi:10.1016/j.cattod.2019.06.071.

13) R. Sesario, K. Dwi, F. Rahmawati, E. Heraldy, and Rachmadani, "Characterization of metal particles on supporting materials mordenite, ultra stable y zeolita, and natural zeolit," in: C. Kusumawardani, A.M.

Abadi, S. Suyanto, I. Wilujeng (Eds.), AIP Conf. Proc., AIP Publishing, Yogyakarta, Indonesia, 2017: p. 020002. doi:10.1063/1.4995088.

14) S.A. Khromova, A.A. Smirnov, O.A. Bulavchenko, A.A. Saraev, V. V. Kaichev, S.I. Reshetnikov, and V.A. Yakovlev, "Anisole hydrodeoxygenation over ni-cu bimetallic catalysts: the effect of Ni/Cu ratio on selectivity," *Appl. Catal. A Gen.*, **470** 261–270 (2014). doi:10.1016/j.apcata.2013.10.046.

15) H. Toraya, "A new method for quantitative phase analysis using x-ray powder diffraction: direct derivation of weight fractions from observed integrated intensities and chemical compositions of individual phases," *J. Appl. Crystallogr.*, **49** (*5*) 1508–1516 (2016). doi:10.1107/S1600576716010451.

16) A. Serafini, L. Lutterotti, S. Gross, and S. Gialanella, "Characterization of nanograined powder samples using the rietveld method applied to electron diffraction ring patterns," *Powder Diffr.*, **32** (*S1*) S63–S68 (2017). doi:10.1017/S0885715617000343.

17) K.D. Nugrahaningtyas, M.M. Putri, and T.E. Saraswati, "Metal phase and electron density of transition metal/HZSM-5," in: AIP Conf. Proc., 2020: p. 020003. doi:10.1063/5.0005561.

18) S. Chaturvedi, P. Shyam, R. Bag, M.M. Shirolkar, J. Kumar, H. Kaur, S. Singh, A.M. Awasthi, and S. Kulkarni, "Nanosize effect: enhanced compensation temperature and existence of magnetodielectric coupling in SMFeO$_3$," *Phys. Rev. B*, **96** (*2*) 1–13 (2017). doi:10.1103/PhysRevB.96.024434.

19) K. Mongkolsuttirat, and J. Buajarern, "Uncertainty evaluation of crystallite size measurements of nanoparticle using X-Ray diffraction analysis (XRD)," in: J. Phys. Conf. Ser., IOP Publishing, 2021: p. 12054. doi:10.1088/1742-6596/1719/1/012054.

20) F. Borchers, H. Meyer, C. Heinzel, D. Meyer, and J. Epp, "Development of surface residual stress and surface state of 42CrMo4 in multistage grinding," in: Procedia CIRP, 2020: pp. 198–203. doi:10.1016/j.procir.2020.02.095.

21) C. Örnek, and D.L. Engelberg, "An experimental investigation into strain and stress partitioning of duplex stainless steel using digital image correlation, x-ray diffraction and scanning kelvin probe force microscopy," *J. Strain Anal. Eng. Des.*, **51** (*3*) 207–219 (2016). doi:10.1177/0309324716631669.

22) T. Imyen, W. Wannapakdee, J. Limtrakul, and C. Wattanakit, "Role of hierarchical micro-mesoporous structure of zsm-5 derived from an embedded nanocarbon cluster synthesis approach in isomerization of alkenes, catalytic cracking and hydrocracking of alkanes," *Fuel*, **254** 115593 (2019). doi:10.1016/j.fuel.2019.06.001.

23) N. Azri, R. Irmawati, U.I. Nda-Umar, M.I. Saiman, and Y.H. Taufiq-Yap, "Promotional effect of transition metals (Cu, Ni, Co, Fe, Zn)–supported on dolomite for hydrogenolysis of glycerol into 1,2-propanediol," *Arab. J. Chem.*, **14** (*4*) 103047 (2021).

doi:10.1016/j.arabjc.2021.103047.

24) O.B. Ayodele, and W.M.A.W. Daud, "Optimization of catalytic hydrodeoxygenation of oleic acid into biofuel using fluoroplatinum oxalate zeolite supported catalyst," *J. Taiwan Inst. Chem. Eng.*, **47** 113–124 (2015). doi:10.1016/j.jtice.2014.09.031.

25) A.A. Ayandiran, P.E. Boahene, A.K. Dalai, and Y. Hu, "Hydroprocessing of oleic acid for production of jet-fuel range hydrocarbons over cu and fecu catalysts," *Catalysts*, **9** (*12*) (2019). doi:10.3390/catal9121051.

26) C.W. Lee, P.Y. Lin, B.H. Chen, R.G. Kukushkin, and V.A. Yakovlev, "Hydrodeoxygenation of palmitic acid over zeolite-supported nickel catalysts," *Catal. Today*, **379** 124–131 (2021). doi:10.1016/j.cattod.2020.05.013.

27) D.P. Upare, S. Park, M.S. Kim, J. Kim, D. Lee, J. Lee, H. Chang, W. Choi, S. Choi, Y.P. Jeon, Y.K. Park, and C.W. Lee, "Cobalt promoted mo/beta zeolite for selective hydrocracking of tetralin and pyrolysis fuel oil into monocyclic aromatic hydrocarbons," *J. Ind. Eng. Chem.*, **35** 99–107 (2016). doi:10.1016/j.jiec.2015.12.020.